



HAL
open science

Impact cutoff frequency – momentum scaling law inverted from Apollo seismic data

Tamara Gudkova, Philippe Lognonné, Katarina Miljković, Jeannine
Gagnepain-Beyneix

► **To cite this version:**

Tamara Gudkova, Philippe Lognonné, Katarina Miljković, Jeannine Gagnepain-Beyneix. Impact cutoff frequency – momentum scaling law inverted from Apollo seismic data. *Earth and Planetary Science Letters*, 2015, 427, pp.57-65. 10.1016/j.epsl.2015.06.037 . insu-03917399

HAL Id: insu-03917399

<https://insu.hal.science/insu-03917399>

Submitted on 1 Jan 2023

HAL is a multi-disciplinary open access archive for the deposit and dissemination of scientific research documents, whether they are published or not. The documents may come from teaching and research institutions in France or abroad, or from public or private research centers.

L'archive ouverte pluridisciplinaire **HAL**, est destinée au dépôt et à la diffusion de documents scientifiques de niveau recherche, publiés ou non, émanant des établissements d'enseignement et de recherche français ou étrangers, des laboratoires publics ou privés.

Impact cutoff frequency – momentum scaling law inverted from Apollo seismic data

Tamara Gudkova ^{a,*}, Philippe Lognonné ^b, Katarina Miljković ^{b,c}, Jeannine Gagnepain-Beyneix ^b

^a *Schmidt Institute of Physics of the Earth RAS, B.Gruzinskaya, 10, 123995 Moscow, Russia*

^b *Institut de Physique du Globe de Paris, Sorbonne Paris Cité, Univ Paris Diderot, CNRS, F-75013 Paris, France,*

^c *Department of Earth, Atmospheric and Planetary Sciences, Massachusetts Institute of Technology, Cambridge, MA 02139-4307, USA.*

ABSTRACT

We perform the analysis of both long and short period data for 40 large meteoroid impacts events gathered by the Apollo lunar seismic network. We extract the linear momentum released by the impact and the cutoff frequency of the recorded seismic spectrum, related to the radiation process of the shock wave generated by the impact. By using a proxy for the local porosity, based on the density of surface craters and well correlated to the most recent GRAIL observations, we demonstrate that the seismic cutoff frequencies for 40 selected impacts correlate with this proxy and therefore likely with the porosity at the impacted areas. Our finding shows that lunar seismic records of meteoroid impacts represent unique geophysical data documenting medium to high-energy (100T~kT TNT yield) impact processes, including the interaction of shock waves with porous media. This work can be applied in the near future to the analysis of the seismic data to be obtained by the InSight mission in 2016 and the investigation of the lateral variations in the Martian regolith.

Key words: Moon, impact processes, cratering, meteorites, Apollo seismic data, regolith

1. Introduction

The seismic detection of impacts on the airless Moon was quite common during the operation of the lunar seismic network with 1753 impact detections reported (Nakamura, 2008). The impact rate depends on the size of the impactors, and was first studied extensively by Oberst and Nakamura (1987, 1991) who proposed an annual rate of impacts given by the relation:

$$\log_{10} N = -0.99 \log_{10} E + 11.4 , \quad (1)$$

where N is the number of event per year, and E is the kinetic energy in J. Assuming an impact velocity of 14 km/s and a seismic coupling efficiency of 10^{-6} (Oberst and Nakamura 1987, 1991), the energy of the largest yearly impact is $10^{11.5}$ J, equivalent to a mass of about 3500 kg.

This is a unique data set, on Earth most of the recorded seismic waveforms from extra-terrestrial bolides are associated with either the atmospheric shock wave or its interaction with the Earth's surface and only a few impacts have generated well-detected P and S waves related to the impact surface (Edwards et al., 2008). The impactors detected by the Apollo long-period (LP) stations have a mass between a fraction of a kilogram to several tons. For impacts at an average speed of 20 km/s (a value more relevant than the one taken by Oberst and Nakamura (1987, 1991) and proposed by Le Feuvre and Wieczorek (2008) from a statistical analysis of the impactors trajectories), the energy released per kg is equivalent to about 48 kg of TNT (1 TNT equivalent to 4.184 GJ). A number of impacts were detected by at least 3 of the 4 stations, enabling the location of the impact. Much smaller mass impactors (on the order of a fraction of a gram) were detected with the short-period (SP) instruments at only one station (Duennebier and Sutton, 1974). When integrated on a global scale, this continuous flux of small impactors has been proposed as the primary source of a continuous micro-seismic noise of the Moon (Lognonné et al., 2009).

Source spectra are typically characterized by a plateau at low-frequencies and a roll-off slope for high-frequency. For quakes, the low-frequency level is proportional to the seismic moment, while it is proportional to the impactor momentum on Lunar seismic records (Lognonné et al., 2009, Gudkova et al., 2011). The high-frequency asymptote is related to the elastic source displacement time history and the form of the radial stress drop field (Denny and Johnson, 1991). The frequency corresponding to the intersection of the low-frequency asymptote and the sloping high-frequency asymptote is called the corner frequency (or cutoff frequency). The cutoff frequency is determined by the source size and material properties of the impacted medium (e.g porosity). This is valid also for nuclear explosions, where the cutoff depends on the geological materials where the explosion occurs (e.g ., Xu et al., 2014).

The largest meteoroid impacts that correspond to impactors with kinetic energies ranging from 0.5 to 1.5 ktons TNT have been recently studied by Gudkova et al. (2011) and they are characterized by the cutoff frequencies ranging from 1 to 1.5 Hz, typically twice lower those expected for nuclear or chemical explosions with comparable yields (Xu et al., 2014). Logically, this lower cutoff frequency seems related to the much lower seismic velocities and densities of the lunar regolith, compared to the bed-rock where nuclear or large chemical explosions occur, but the systematic and complete analysis of the relation between the seismic impulse (or momentum) and cutoff frequency of the Apollo seismic observations has never been performed.

In this paper, we report for the first time the observational constraints on the cutoff frequency-momentum scaling law, which will be crucial for estimating the size of impactors for future seismic monitoring on the Moon, Mars and other planetary bodies with thin or no

atmosphere. This study is based on the Apollo seismic data and the crater density on the lunar surface. In addition to the first theoretical analysis of the observed dependence of the cutoff frequency, we also provide observational evidences on the sensitivity of the cutoff frequency to the regolith porosity.

2. Analysis of meteoroid impacts recorded by the Apollo seismometers

We have performed the analysis of 40 large meteoroid impacts located in different regions (Table 1 and Fig.1) and recorded by the Apollo network during the 1970s on both LP and SP vertical components of the seismic instruments from up to three stations. The four Apollo seismometers operating as a network were extremely sensitive, capable of detecting displacements of 3×10^{-10} m at frequencies between 0.1 and 1 Hz on the LP instrument in flat response mode, 0.5×10^{-10} m at 0.45 Hz for the LP instrument in peaked response mode, as well as 0.5×10^{-10} m at 8 Hz for the SP instrument (Lammlein et al., 1974). In addition to the very low environmental noise and low attenuation, the Apollo seismic network acted as an efficient impact detector (e.g. McGarr et al., 1969, Oberst and Nakamura, 1987, Lognonne et al., 2009, Kawamura et al., 2011, Yamada et al., 2011). An example of waveforms for a natural impact is shown in Fig. 2.

When a meteoroid impacts the Moon, its linear momentum is transferred into the target and its kinetic energy is distributed between heating and fracturing of the target with a small fraction of energy (of the order of 10^{-4} - 10^{-6}) being transferred into shock and seismic waves. The seismic efficiency of an impact, defined as the ratio of seismic energy over the impactor kinetic energy, depends on meteoroid characteristics such as mass, composition, velocity and impact angle, as well as on the properties of the target material (McCarr et al., 1969, Lognonné et al., 2009), which could vary substantially between the highlands and the maria. Meteoroid impacts are well explained by the seismic impulse approach method, which integrates both the impactor and the ejecta momentum (Lognonné et al., 2009; Gudkova et al., 2011). This method has been calibrated with artificial impacts with known mass and impact velocities and the source function model. It allows us to retrieve the mass of the impactor within 20% of the real mass. In this paper we focus our study on the source function, as recorded by the Apollo seismometers, and use the same method and model as described in Gudkova et al. (2011). This model fits both impacts: an impact at a short distance and an impact at a long distance, and allows the analysis of meteoroid impacts events occurring both in the lunar maria and highlands regions as demonstrated below.

The seismic source of an impact is related to the pressure glut generated by the shock wave, as described by Lognonné et al (1994). The associated seismic moment can be expressed as

$$\text{[Broken image placeholder]} \quad (2)$$

where ε_{ij} is the strain tensor of the Green function defined as $\text{[Broken image placeholder]}$, where \mathbf{G} is the Green function displacement field. Π_{ij} is the pressure glut tensor, defined as

$$\text{[Broken image placeholder]} \quad (3)$$

where P is the pressure, κ the bulk compressibility, \mathbf{u} and \mathbf{v} are the displacement and the velocity fields, respectively. Repeated indices imply summation. During the strong non-linear regime of the shock wave propagation, the generated pressure is much larger than the Hooke equivalent pressure of the generated deformation ($\text{[Broken image placeholder]}$). Therefore, the pressure glut can be assumed to be equal to

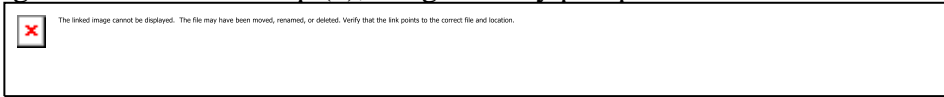
$$\text{[Broken image placeholder]} \quad (4)$$

and verify the momentum equation:



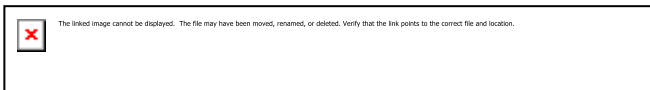
(5)

where $\boldsymbol{\pi} = \rho \mathbf{v}$ is the volumetric distribution of the linear momentum in the shocked area. Applying Gauss theorem to Eq. (2), integration by part provides



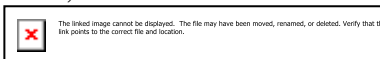
(6)

where \mathbf{G} is the Green function displacement field and the surface integral cancels at the surface delimiting the shocked-area where no seismic source is present anymore. At long period, the wavelength and therefore the typical space scale of the Green displacement function G is large with respect to the size of the shocked area, and Eq. (6) can be expressed as



(7)

where $I(t)$ is the linear momentum of the shocked area during the shock regime. By conservation of the momentum, the latter is equal to the momentum of the impactor minus the momentum of the ejecta, as described by Lognonné et al (2009). When the duration of the shock is neglected, the function $I(t)$ is proportional to an Heaviside function, while in the general case, it can be written as



(8)

where $g(t)$ is the source function and $*$ is the convolution product. It is known that the displacement spectrum generated by a quake is flat in displacement and $\sim \omega^2$ in acceleration (Aki and Richards, 2002). The time derivative in Eq. (7) shows that for an impact these spectra are $\sim \omega$ and $\sim \omega^3$ in displacement and acceleration, respectively; still all spectra are proportional to the impulse, as observed on the lunar impact data (Lognonné et al., 2009).

The source function $g(t)$ contains all departures from the long-period, strong shock wave regime and integrates:

- (i) the weak regime of the shock, when the pressure glut is only slightly larger than the Hooke pressure (Eq. (5)), which terminates the radiation of the shock wave,
- (ii) the non finite character of the source, especially when the shock waves grows (Eq. (7)).

In order to extract the finite time of the impact, we consider the following seismic source function for modeling an impact occurring at time $t=0$ and location \mathbf{x}_s :

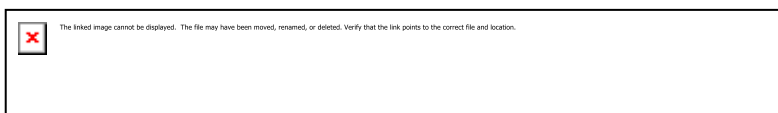
$$I(t, \mathbf{x}) = S m \mathbf{v} \delta(\mathbf{x} - \mathbf{x}_s) g(t) = S \mathbf{f}(t) \delta(\mathbf{x} - \mathbf{x}_s) = S \mathbf{F}_0(t, \mathbf{x}) * g(t), \quad \mathbf{F}_0(t, \mathbf{x}) = m \mathbf{v} \delta(t) \delta(\mathbf{x} - \mathbf{x}_s)$$

$$g(t) = 1 + \cos \omega t \text{ for } -\pi / \omega < t < \pi / \omega,$$

$$g(t) = 0 \text{ otherwise,} \quad (9)$$

where we introduce the amplification factor S , whose value depends on the impact velocity and is typically about 2 (Lognonné et al., 2009), the time dependence of the source $g(t)$, and the time constant τ , equal to  to denote the time-duration of the seismic excitation

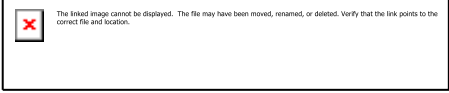
process. The Fourier transform of $g(t)$ is the sum of sinc functions ($\text{sinc}(x) =$ ):



(10)

Its asymptotic form for frequencies much higher than ω_1 is proportional to  and therefore ω^{-3} , as the asymptotic form of sinc function is ω^{-1} . At low frequency, it is constant as the limit of sinc function is 1 at zero frequency. This model therefore provides a seismic acceleration spectral density varying as ω^3 at low frequency and flat after the cutoff frequency.

The amplitude of the acceleration spectrum recorded at a given epicentral distance can be approximated as (Lognonné et al., 2009, Gudkova et al., 2011)



$$(11)$$

where B is a constant depending on the seismic impulse and epicentral distance, Q is the quality factor related to attenuation and t_{prop} is the propagation time of the waves. The bracketed term corresponds to the Green's function response.

The best least squares fit of the logarithmic amplitudes for Q, τ and B in Eq. (11) are obtained by a grid search. The recordings of meteoroid impacts are well explained by the model for the seismic source that includes the seismic impulse from the impactor and the ejecta, and as well as the effects of the attenuation of the seismic waves. Figure 3 shows the results for the best values for Q, τ and B for the impacts that occurred on May 23rd, 1971 and on June 28th, 1977 (we use a simpler notation, here 19710523 and 19770628) ($Q > 20000$; $\tau = 0.45$ and 1.3 s, respectively). We get a very good fit to the data, with a 94% variance reduction and a very high quality factor, too high to be constrained with confidence, which explains the use of a lower bound. The impact 19710523 takes place in the highlands region, far a way from the stations (green line, Fig. 3), while 19770628 impacted into the lunar maria, near the stations (blue line, Fig. 3). As seen in the Fig. 3, the source function (Eq. (11)) fits both impacts: an impact at a short distance and an impact at a long distance, as well as whether an impact is in two geologically diverse regions.

The date of the events, their latitude, longitude, seismic impulses (defined as meteoroid momentum) of the events and the time-duration of the excitation process are listed in Table 1. Most of the impacts that were considered in this study occurred on the lunar nearside hemisphere. A limited number of seismic recordings of impacts on the east farside hemisphere were made at large epicentral distances from the Apollo network that is located on the nearside hemisphere (Fig. 1).

3. Impact cutoff frequency - momentum relation

Let us compare the impact momentum and the cutoff frequency (or the time-duration of the seismic excitation process τ) (Table 1 and Fig. 4) on a log-log scale and determine the power law relationship between these two parameters, such that $\tau = \tau_0 (mv/10^7)^\beta$, where m, v are the mass (kg) and velocity of the impactor (m/s), τ (in s) is the cutoff time and β is the scaling power. The latter is obtained by least square fit of the data set for the momentum transfer of the impactor and seismic impact duration.

We find that the values for the time-duration of the seismic excitation process for all data sets (black line, Fig. 4) are described reasonably well by a power law dependence on the seismic moment with $\tau_0 = 0.65$ s and a power of about 0.14 (with a root-mean-square error of 16 %), suggesting that the cutoff frequency increases by a factor of 1.40 when the impulse increases by an order of magnitude. (Other lines in Fig. 4 will be discussed in Section 5). This value of β is slightly smaller than the one found for nuclear or large chemical explosions,

such as the hydrodynamic simulations of Xu et al. (2014), for which the cutoff time increases by a factor of about 1.5 for a yield increase of 10, between 0.5 kT and 5 kT.

Contrary to the magnitude-cutoff relation for nuclear tests (e.g. Mueller and Murphy, 1971, Murphy and Mueller, 1971) for which numerous publications exist, very little information on impacts in the kT range is available. Laboratory tests of high velocity impacts do not reach the kiloton of TNT range because it is too dangerous: typical impactor velocities are usually in excess of 7.5 km/s with masses around a few 10's of grams. Thus, only theoretical approaches can address this problem before the development of hydrodynamics modeling comparable to those performed for nuclear explosions (e.g. Xu et al., 2014).

Two theoretical approaches are used to model the observations: one is based on analytical energy balance models while the other is based on numerical solutions of the fundamental dynamic equations. We take the first one. Let us then consider a planar shock wave progression through undisturbed media that can be described using the so-called Hugoniot-Rankine equations (e.g. Melosh, 1989), in which the equations of the conservation of mass, momentum and energy, and the equation of state of the material must be satisfied.

The conservation of mass is defined as

$$\rho_0 U = \rho_1 (U - u_p) \quad (12)$$

where U is the shock wave velocity, u_p is the particle velocity, grain density ρ_0 and bulk density ρ . Adding porosity ϕ reformats the equation (12) to

$$\rho_0 U = \rho (1 - \phi) (U - u_p) \quad (13)$$

Combining the conservation of momentum with Eq.13 and assuming that $P_0 \ll P$, because P_0 is the pressure in the near-surface undisturbed media, but also much lower than the pressure P imposed by the passing shock wave, we have

$$P = \rho_0 U u_p \quad (14)$$

The power law in the pressure decay regime can be approximated as $P = A \left(\frac{r}{R_{pr}} \right)^{-n}$, where the distance from the impact point r is normalized to the projectile radius R_{pr} , and A is a constant (Pierazzo et al., 1997). Since material properties have small influence on n , we adopt its value to be 1.55 from Pierazzo et al. (1997) (where the reported value for n is valid for impacts at the impact velocity of 20 km/s). Combining the pressure decay relationship with Eq.14 we get

$$P = A \rho_0 U u_p \left(\frac{r}{R_{pr}} \right)^{-1.55} \quad (15)$$

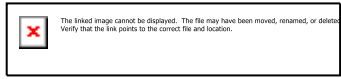
As one length scale we consider the thickness of the shock wave, assuming that the shock wave progression is equalized by hydrostatic pressure such that $\rho_0 U^2 = P$, we get two variations

$$r = \left(\frac{A \rho_0 U u_p}{P} \right)^{0.64} R_{pr} \quad \text{or} \quad r = \left(\frac{A \rho_0 U u_p}{P} \right)^{0.64} R_{pr} \quad (16)$$

The other scale is the duration of the shock wave, which can be defined as

$$\tau = \frac{r}{U}$$

Substituting $U(r)$ from Eq. 15 and r from Eq. 16 in $t(r)$ and assuming the porosity is constant we come to the relation



(17)

where m_i is the mass of the impactor. For 20 km/s impactor velocity, we have m_i of about 0.1 which is a value comparable (but smaller) to the value of 0.14 found by the least square fitting of all data sets.

A more careful analysis of Fig. 4 demonstrates that small impacts show much smaller scatter in the data than larger ($I > 10^8$ Ns) impacts, for which the source duration can vary by a factor of nearly 2.5 (from 0.60 to 1.60 s). As seismic P wave velocity is typically about 1 km/s in the upper layer of the Moon (e.g. Vinnik et al., 2001, Nakamura, 2011), large impacts are likely to be sensitive to the properties of the upper subsurface and it can be expected that areas with high porosity will have, for an impact with the same impulse, a larger source time, due to a slower propagation of the impact shock waves. As shown in Fig.1, the impacts are sampling very different areas on the Moon, from mare basalts to highlands regions. Therefore, significant variations in the regolith properties can be expected to exist, depending on the surface impact cratering history.

4. Estimating the regolith porosity in the vicinity of the impacts

Porosity is a poorly known parameter. The latest porosity map derived from the GRAIL gravity measurements (Wieczorek et al., 2013) provided estimates of porosity in the farside highlands but not in the nearside maria regions. In this study, we use an indirect proxy to the porosity, based on the impact history of this region.

Regolith is generated and sustained by the constant meteoroid bombardment, a process that fractures and ejects surface material. During the early impact bombardment, when the largest impact events on the Moon had occurred, the lunar mega-regolith layer (e.g. Hartmann et al., 2000) was formed. Subsequently, mega-regolith has been continuously bombarded by smaller impact events, which contributed to the formation of the upper-most finely grained regolith layer.

Previous models for mixing and distribution of ejecta from impact craters and basins were developed based on terrestrial and lunar craters (McGetchin et al., 1973; Pike, 1974) as well as impact scaling laws (e.g. Housen et al., 1983; Housen and Holsapple; 2011). Mixing of the material during ejecta emplacement has been used in previous studies to estimate the amount of emplaced material at locations such as the Apollo 16 site (e.g. Petro and Pieters, 2006) and the South Pole-Aitken basin (Petro and Pieters, 2004). Their absolute value results were highly sensitive to the choice of the ejecta mixing model. However, the relative portion of regolith emplaced during basin formation was independent of the model, assuming homogenous mixing (Petro and Pieters, 2006).

We introduce a new function, impact-regolith function approximated to be proportional to the sum of the ejecta created by a number of successive impacts on the lunar surface. Areas with higher crater density are expected to have deeper regolith than the areas with lower crater density. Due to the complex nature of impact ejecta emplacement presented in previous studies, the impact-regolith function used here is considered as a relative measure of the regolith maturity: it is correlated with the porosity and the thickness of regolith as well as the shear velocity of the subsurface layers. In our approach, this function is directly related to the final (present day) thickness of the regolith and we will discuss it as such.

The impact-regolith function is calculated as the sum of the ejecta from the lunar craters between 20 and 500 km in diameter (http://www.planetary.brown.edu/html_pages/data.htm) catalogued by Head et al. (2010) and Kadish et al. (2011). Our model assumes a uniform distribution of ejecta around each crater and no mixing of ejecta layers. We do not consider a small number of craters larger than 500 km under assumption that the ejecta from those impacts would have global effects to the Moon that formed the oldest and deepest mega-regolith, which have been buried and compacted by subsequent impacts.

We use the impact model of Housen et al. (1983) and Holsapple (1993) and the HTML software available at <http://www.keith.a.washington.edu/craterdata/scaling/index.htm>, to calculate the crater diameter and depth for a range of impact parameters. Then, the ejecta volume for a given crater diameter is approximated as:

$$\begin{aligned} V_{\text{ejecta}} \text{ (in km}^3\text{)} &= 0.0937 D^3 + 0.0406 D^2 - 1.825 D + 14.8743, & \text{for } 10 < D < 100 \text{ km,} \\ V_{\text{ejecta}} \text{ (in km}^3\text{)} &= 0.0001 D^2 - 0.02 D + 1.3438, & \text{for } 100 < D < 500 \text{ km,} \end{aligned} \quad (18)$$

The output from the model is shown in Table 2 and it contains estimates of the excavation mass, the volume of material ejected and the depth of the crater, for a given crater diameter.

The estimates of the radial deposition of the ejecta blanket produced by a single impact, and the ejection velocity are related by the ballistic equation:

$$r = x + \frac{v^2 \sin^2(\theta)}{g}, \quad (19)$$

where θ is the launch angle (assumed to be an average of 45°), x is an initial ejecta launch position, v is the impactor velocity (assumed to be 20 km/s) and g is the gravitational acceleration.

Combining Eq. (19) with the calculated ejecta volumes (V_{ejecta}) (Eq. (18)), we estimated the radial distribution of the ejecta thickness in percentages, for a given impact (Table 3). Our model for the ballistic deposition of impact ejecta for a single crater is represented by two components. The central component is defined as a cylindrical core around the impact point that contains 50% of ejecta volume (V_{ejecta}). Its radius is equal to twice the radius of the crater (or one crater diameter D). The second component of the ejecta thickness distribution contains the volume ejected beyond this range $r_{\text{ej}} = D$, which is interpolated as

$$V(r), \% = D * \frac{V_{\text{ejecta}}}{2r} \quad (20)$$

We neglect the ejecta material at the distances larger than ten times the crater diameter, as the amount of the ejecta beyond this limit is less than 5%. By applying this calculation to all lunar craters considered in this study and by rigidly stacking the ejecta layers without mixing, we approximated the distribution of the global lunar regolith thickness. Considering the simplifications used in this approach, we define the obtained distribution as a proxy estimates for the impact-regolith function that is proportional to the real regolith thickness over the entire Moon. Figure 5 shows the locations of the meteoroid impact events recorded by the Apollo seismic stations (listed in Table 1) on the map of the proxy estimates for crustal porosity as described above and the contour of the GRAIL coverage from Wieczorek et al. (2013).

Our porosity estimates are consistent with the GRAIL-derived crustal porosity by Wieczorek et al. (2013). Sixteen impacts are located within the contour of GRAIL coverage. As seen in Fig. 6, a rather large misfit is obtained for impacts 15, 27, 32, 36, 39 and 40. As seen from the map in Fig. 5, these impacts are located in the areas where the impact-regolith function (or regolith depth and also the porosity) is highly variable over short distances. If we use the variability of the impact regolith function within the impact location error ellipses from seismic data (2-4 degrees along latitude or longitude), shown by error bars in Fig.6, these impacts will fit well the correlation line (with a root-mean-square error of 27%).

In addition, our results are also in agreement with regolith thickness estimates from radar optical data (Shkuratov, Bondarenko, 2001), crater morphology (Bart et al., 2011, Head et al., 2010). Its analysis shows that the regolith thickness in the lunar Maria region is, on average, half the thickness than in the non-mare regions. The regional variations of the regolith thickness are almost the same for lunar maria and highlands, although the average regolith thickness is larger in the highland region by a factor of two (5 and 12 m) (Shkuratov and Bondarenko, 2001).

Below our proxy estimates for crustal porosity is used for detecting the general trend of sensitivity of seismic cutoff frequencies to the surface geology in the impact region.

5. Trade-off between seismic source parameters and the regolith maturity

By comparing impact momentum, its cutoff frequency (or the time-duration of the seismic excitation process) (Table 1) and the location of the events (Fig. 1), we find that the larger the impact, the lower the cutoff frequency, for the impacts occurring in the same surface area. Nevertheless, among impacts in different regions, this is not necessary valid. We assume that the difference between the source cutoff frequencies for the impacts with the same momentum are caused by excitation processes in different geologic regions (the lunar maria and highlands) and therefore by deceleration or acceleration of the shock wave associated with the collapse of subsurface porosity.

Let us go back to Fig. 4 and analyze the relationship between the impact duration, the momentum transfer of the impactor and the thickness of the lunar regolith in the vicinity of the impact (or the impact-regolith function, a proxy that estimates crustal porosity obtained using the crater density in Section 4). As noted above, the seismic impact duration for all impacts under consideration can be approximated by a power law $\tau = \tau_0(mv/10^7)^\beta$ with $\tau_0 = 0.65$ s and $\beta = 0.14$ (black line). For our analyses, we divided the available data sets into three groups, depending on the regolith thickness in the vicinity of the impact: the minimum, the mean, and the maximum regolith thickness. The first group involves impact events located where the impact-regolith function is between 0 and 8, the second group between 8 and 13, and third group between 13 and 20. Color lines in Fig. 4 display the least squares solution for the power law dependence of the cutoff frequency (or the time-duration of the seismic excitation process τ) for each group. The power law fit in first group yields values of $\tau_0 = 0.6$ s and $\beta = 0.04$ (blue line, impact-regolith function is between 0 and 8), second group: $\tau_0 = 0.67$ s and $\beta = 0.12$ (green line, impact-regolith function is between 8 and 13), and the third group: $\tau_0 = 0.64$ s and $\beta = 0.21$ (red line, impact-regolith function is between 13 and 20), with a root-mean-square error of 13%, 25%, 14%, respectively. Our goal was mainly limited to modeling the variation in the cutoff frequency with the regolith porosity in the vicinity of the impact. Figure 4 shows that the larger the impact, the higher the impact duration and the slopes of the lines increase with the increase of the regolith thickness (the scaling power β is increasing with the regolith thickness).

5. Conclusion

Our study confirms that the lunar impacts are characterized by a low cutoff frequency related to the propagation of the shock wave in an impacted subsurface and suggests a dependence of the cutoff frequency on both the impact linear momentum and the porosity (or seismic velocity) of the shocked area.

The lower the time-duration of the process, the less is the maturity of the regolith. Seismic cutoff frequencies, obtained from the Apollo seismic recordings for the 40 meteoroid

impacts, depend not only on the impact size, but also on the impact location, as the seismic radiation of the shock wave progression depends on the properties of the most-upper regolith layers. An overlay of the observed seismic cutoff with the map of the lunar regolith distribution shows that there is indeed a correlation between the regolith depth and the seismic cutoff frequency of an impact event.

Despite the relatively bad quality of the lunar Apollo data in term of bandwidth and resolution and the lack of detailed model of the lunar crust and upper mantle, this correlation between the seismic data and the regolith structure on the Moon opens perspectives in the remote determination of the lunar structure by seismic methods, which might be used by future studies investigating the 3D structure of not only the lunar crust (Chenet et al., 2006; Yamada et al., 2011), but also of the most upper regolith layers.

This work will be particularly important for new studies of Mars, for which landing of a seismic station is planned with the InSight mission in September 2016. Although the recording of quakes will be the primary target of the seismic monitoring (e.g. Panning et al., 2015), several impacts detections per year are also expected (e.g. Lognonné and Johnson, 2007). This work can be applied to the analysis of these future impact seismic data and might enable remote investigation of the lateral variations in the Martian regolith.

Acknowledgements. We thank Sharon Kedar and anonymous reviewer for constructive comments and suggestions which helped improving the manuscript. This work was supported by the French Space Agency CNES. This research was made possible partly by Grant No. 15-02-00840 from the Russian Foundation for Basic Research. T.V.Gudkova thanks also IPGP for the possibility to work for a short time in the Equipe Planétologie et Sciences Spatiales, Institut de Physique du Globe de Paris during which time this research was made. Katarina Miljković's work is supported by UnivEarthS LabEx project of the University of Sorbonne Paris Cité grants ANR-10-LABX-0023 and ANR-11-IDEX-0005-02. This is IPGP contribution number XXX.

References:

- Aki, K., Richards, P.G., 2002. Quantitative Seismology, second ed. Univ. Sci. Books, Sausalito, CA. 700pp.
- Bart, G.D., Nickerson, R.D., Lawder M.T., Melosh, H.J. 2011. Global survey of lunar regolith depths from LROC images. *Icarus* 215, 485–490.
- Chenet, H., Lognonné, P., Wieczorek, M., Mizutani H. 2006. Lateral variations of lunar crustal thickness from Apollo seismic dataset. *Earth Planet. Sci. Lett.* 243, 1–14.
- Denny, M.D and Johnson, R.L. 1991. The explosion seismic source function: models and scaling laws reviewed, in : Explosion Source Phenomenology, Geophysical Monograph, (Eds. S. R Taylor, H. J Patton and P.G Richards), American Geophysical Union : Washington, DC, USA, 65, p. 1-24.
- Duennebieer, F., Sutton, G.H. 1974. Meteoroid impacts recorded by the short-period component of Apollo 14 Lunar Passive Seismic station. *J. Geophys. Res.* 79, 4365–4374.
- Edwards, W.N., Eaton, D.W., Brown, P.G. 2008. Seismic observations of meteors: coupling theory and observations. *Rev. Geophys.* 46, 1-21.
- Gudkova, T. V., Lognonné, Ph., Gagnepain-Beyneix, J. 2011. Large impacts detected by the Apollo seismometers: impactor mass and source cutoff frequency estimations. *Icarus* 211, 1049–1065.
- Hartmann, W. K., Ryder, G., Dones, L., Grinspoon, D., 2000. The time-dependent intense bombardment of the primordial Earth/Moon system. In: Origin of the Earth and Moon (Eds. R. M. Canup, K. Righter et al.), University of Arizona Press, Tucson, USA, 493–512.
- Head, J.W., Fassett, C.I., Kadish, S.J., Smith, D.E., Zuber, M.T., Neumann, G.A., Mazarico, E. 2010. Global distribution of large lunar craters: Implications for resurfacing and impactor populations. *Science* 329, 1504–1507.
- Holsapple, K. A. 1993. The scaling of impact processes in planetary sciences. *Annu. Rev. Earth Planet. Sci.* 21, 333–373.
- Housen, K. R., Schmidt, R. M., Holsapple, K. A. 1983. Crater ejecta scaling laws: Fundamental formes based on dimensional analysis. *J. Geophys. Res.* 88, 2485–2499.
- Housen, K. R., Holsapple, K. A. 2011. Ejecta from impact craters. *Icarus* 211, 856-875.
- Kadish, S.J., Fassett, C.I., Head, J.W., Smith, D.E., Zuber, M.T., Neumann, G.A., Mazarico, E. 2011. A global catalog of large lunar crater (≥ 20 km) from the Lunar Orbiter laser Altimeter, 42nd Lunar Planet. Sci. Conf. abstr.1006
- Kawamura, T., Morota, T., Kobayashi, N., Tanaka, S., 2011. Cratering asymmetry on the Moon: New insight from the Apollo Passive Seismic Experiment, *Geophys. Res. Lett.*, **38**, L15201, doi:10.1029/2011GL048047
- Lammlein, D.R., Latham, G.V., Dorman, J., Nakamura, Y., Ewing, M. 1974. Lunar seismicity, structure, and tectonics, *Rev. Geophys.* 12, 1-21.
- Lammlein, D.R. 1977. Lunar seismicity and tectonics. *Phys. Earth Planet. Inter.* 14, 224–273.
- Lognonné P. and C.Johnson, 2007. Planetary Seismology, in « Treatrise in Geophysics, 10, Planets and Moons », editor G.Shubert, chapter 4, 69-122, Elsevier, 2007, doi : [10.1016/B978-044452748-6.00154-1](https://doi.org/10.1016/B978-044452748-6.00154-1),
- Lognonné, Ph., Le Feuvre, M., Johnson, C.L., Weber, R.C. 2009. Moon meteoritic seismic hum: steady state prediction. *J. Geophys. Res.* 114, E12003.
- Lognonné, P, Mosser, B., Dahlen, F.A., 1994. Excitation of the Jovian seismic waves by the Shoemaker-Levy 9 cometary impact, *Icarus*, **110**, 186-195, doi : [10.1006/icar.1994.1115](https://doi.org/10.1006/icar.1994.1115) .
- Le Feuvre, M., Wieczorek, M.A., 2008. Nonuniform cratering of the terrestrial planets, *Icarus*. 197. 291-306.
- McGarr, A., Latham, G.V., Gault, D.E., 1969. Meteoroid impacts as source of seismicity on

- the Moon. *J. Geophys. Res.* **74** (25), 5981-5994.
- McGetchin, T.R., Settle, M., Head, J.W. 1973. Radial thickness variations in impact crater ejecta : Implications for Lunar basin deposits. *Earth Planet. Sci. Lett.* **20**, 226–236.
- Melosh, H. J. 1989. *Impact Cratering. A Geological Process.* Oxford Monographs on Geology and Geophysics, Oxford University Press, New York, USA, 245 pp.
- Mueller, R.A., Murphy, J.R. 1971. Seismic characteristics of underground nuclear detonations. Part I. Seismic spectrum scaling. *Bull.Seism.Soc.Am.* **61**, N6, 1675-1692.
- Murphy, J.R., Mueller, R.A., 1971. Seismic characteristics of underground nuclear detonations. Part II. Elastic energy and magnitude determinations. *Bull.Seism.Soc.Am.* **61**, N6, 1693-1704.
- Nakamura, Y. 2008. Catalog of seismic events recorded by Apollo mission, University of Texas (<ftp://ftp.ig.utexas.edu/pub/PSE/catsrepts/>).
- Nakamura, Y. 2011. Timing problem with the Lunar Module impact data as recorded by the LSPE and corrected near-surface structure at the Apollo 17 landing site. *J.Geoph.Res.* **116**, E12005, doi:10.1029/2011JE003972, 2011
- Oberst, J., Nakamura, Y., 1987. Distinct meteoroid families identified on the lunar seismograms, *J. Geophys. Res.*, **92**, 769–773.
- Oberst, J., Nakamura, Y., 1991. A search for clustering among the meteoroid impacts detected by the Apollo lunar seismic network, *Icarus*, **91**, 315–325.
- Panning, M.P., E. Beucler, Drilleau, Mocquet, Lognonné, P, Banerdt, W.B., 2015. Verifying single-station seismic approaches using Earth-based data: Preparation for data return from the InSight mission to Mars, *Icarus*, **230-242**, **248**, doi : 10.1016/j.icarus.2014.10.035.
-
- Petro, N.E., Pieters, C.M. 2004. Surviving the heavy bombardment: Ancient material at the surface of South Pole-Aitken Basin. *J. Geophys.Res.* **109**, E06004, doi:10.1029/2003JE002182.
- Petro, N.E., Pieters, C.M. 2006. Modiling the provenance of the Apollo 16 regolith. *J.Geophys.Res.* **111**, E09005, doi:10.1029/2005JE002559.
- Pierazzo A., Vickery A.M., Melosh H.J. 1997. A réévaluation of impact melt production. *Icarus.*,**127**, 408–423.
- Pike, R.G. 1974. Ejecta from large craters on the Moon : Comments on the geometric model of McGetchin et al. *Earth Planet. Sci. Lett.* **23**, 265–274.
- Shkuratov, Y.G., Bondarenko, N.V. 2001. Regolith layer thickness mapping of the Moon by radar and optical data. *Icarus* **149**, 329–338.
- Smith, D.E. Zuber, M.T., Jackson, G.B., Cavanaugh, J.F. Neumann, G.A., Riris, H., Sun, X., Zellar, R.S., Coltharp, C., Connelly, J., Katz, R.B., Kleyner, I., Liiva, P., Matuszeski, A., Mazarico, E.M., McGarry, J.F., Novo-Gradac, A-M., Ott, M.N., Peters, C., Ramos-Izquierdo, L.A., Ramsey, L., Rowlands D.D., Schmidt, S., Scott III, V.S., Shaw, G.B., Smith, J.C., Swinski, J-P., Torrence, M.H., Unger, G., Yu, A.W., Zagwodzki, T.W. 2010. The Lunar Orbiter Laser Altimeter investigation on the Lunar Reconnaissance Orbiter mission. *Space Sci. Rev.* **150**, 209.
- Vinnik L.P., Chenet H., Gagnepain-Beyneix J., Lognonné Ph. 2001. First seismic receiver functions on the Moon. *Geophys. Res. Lett.* **28**, 3031–3034.
- Wieczorek M.A., Neumann, G.A., Nimmo, F., Kiefer, W.S., Taylor, G.J., Melosh, H.J., Phillips, R.J., Solomon, S.C., Andrews-Hanna, J.C., Asmar, S.W., Konopliv, A.S., Lemoine, F.G., Smith, D.E., Watkins, M.M., Williams, J.G., Zuber, M.T. 2013. The crust of the Moon as seen by GRAIL. *Science.* **339**, 671–675.
- Xu, H., Rodgers, A.J., Lomov, I.N., Vorobiev, O.Y. 2014. Seismic source characteristics of nuclear and chemical explosions in granite from hydrodynamic simulations. *Pure Appl. Geophys.* **171**, 507–521

Yamada, R., Garsia, R.F., Lognonné, P., Le Feuvre, M., Calvet, M., Gagnepain-Beyneix, J. 2011. Optimisation of seismic network design: application to a geophysical international lunar network. *Planet. Space Sci.* 59, 343–354.

Figure captions:

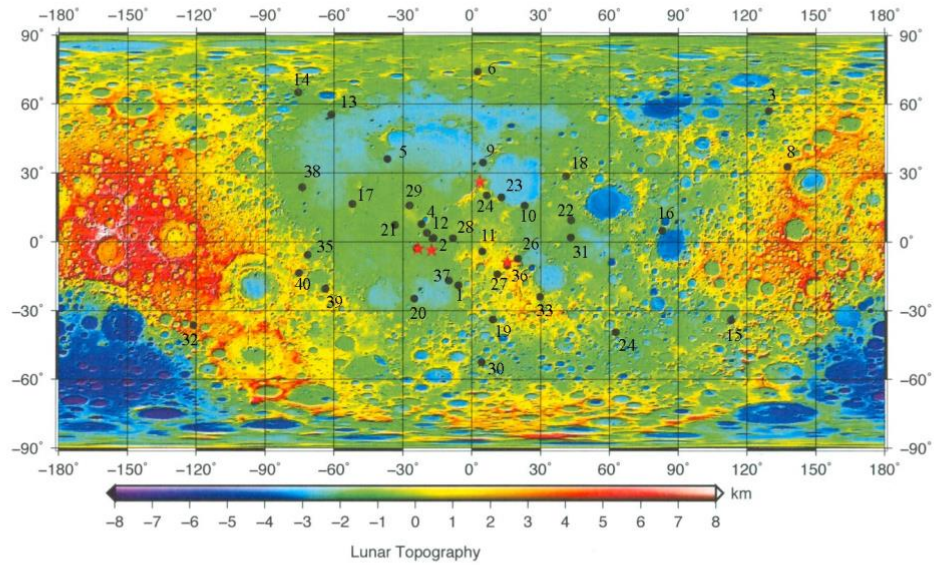


Fig. 1. Locations of studied meteoroid impacts and the Apollo seismic stations imposed on the lunar topography map obtained by the Lunar Orbiter Laser Altimeter (LOLA) onboard the Lunar Reconnaissance Orbiter (LRO) (*Smith et al., 2010*).

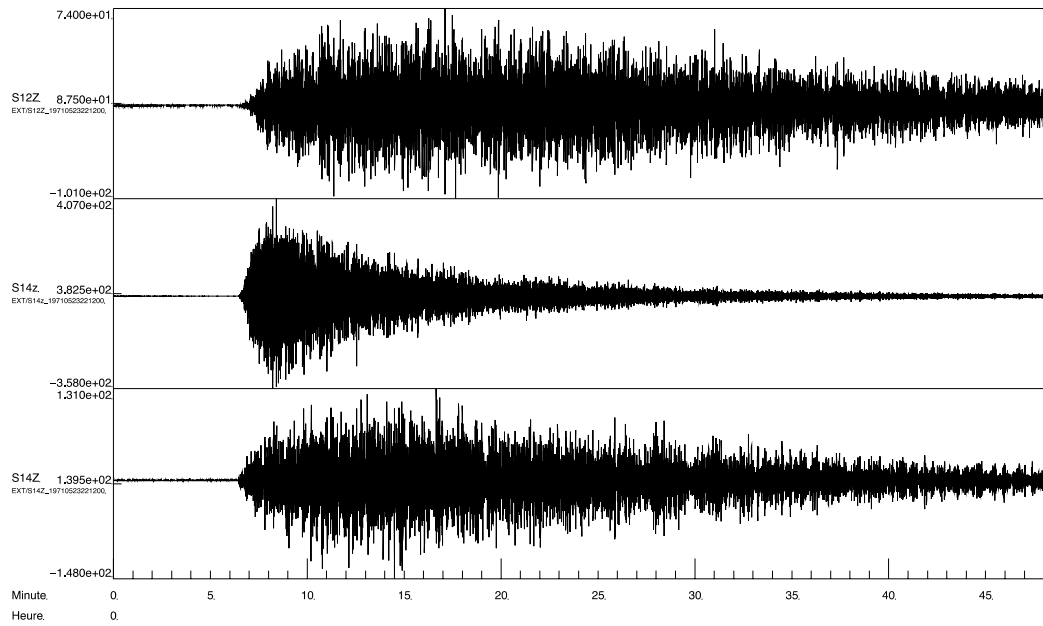


Fig. 2. An example of waveforms for natural impact, the 23rd of May 1971 (19710523), recorded on both long-period Z and short-period z vertical channels by the Apollo Passive Seismic Network. The record span 50 min, x-axis time is in minutes, y-axis is in digital units. From the top down: station 12 long-period (S12Z), station 14 short-period (S14z) and station 14 long-period (S14Z).

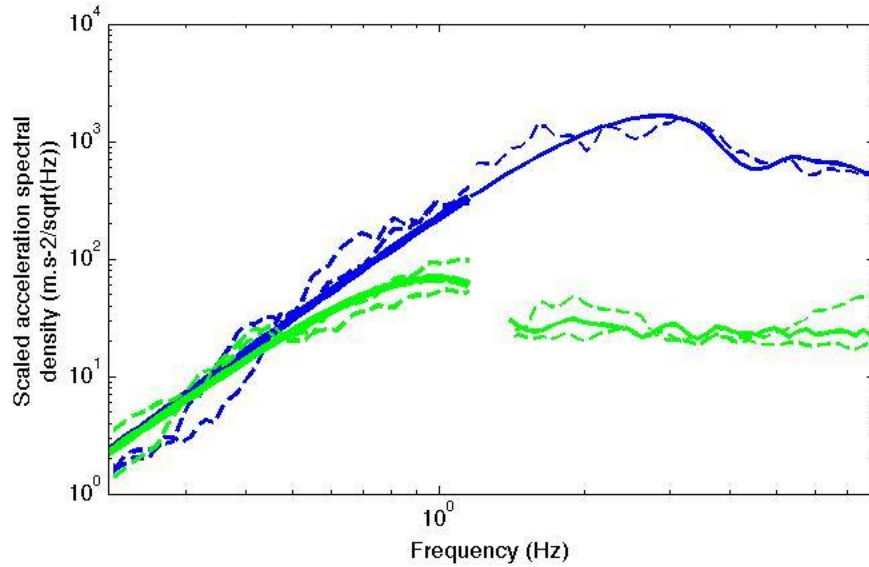


Fig. 3. Log-log plot of scaled acceleration spectral density for two meteoroids impacts: (blue dashed lines) meteoroid impact event 19710523 recorded on long-period (L) and short-period (z) vertical components at the Station 14 (S14), and on long-period vertical component at the Station 12 (S12); and (green dashed lines) meteoroid impact event 19770628 recorded on long-period vertical component (L) at stations 12 and 15, and on short-period vertical components (z) at stations 14 and 16; (blue and green solid lines) calculated scaled acceleration spectral densities for meteoroid impact events 19710523 and 19770628, respectively. In addition to the seismic impulse scaling, the attenuation effect has been corrected by multiplying the spectrum by $\exp\left(\frac{\omega t_{prop}}{2Q}\right)$, where Q is the quality factor found by the least squares inversion, $Q=20000$. A gap in the green line is the lack of SP data.

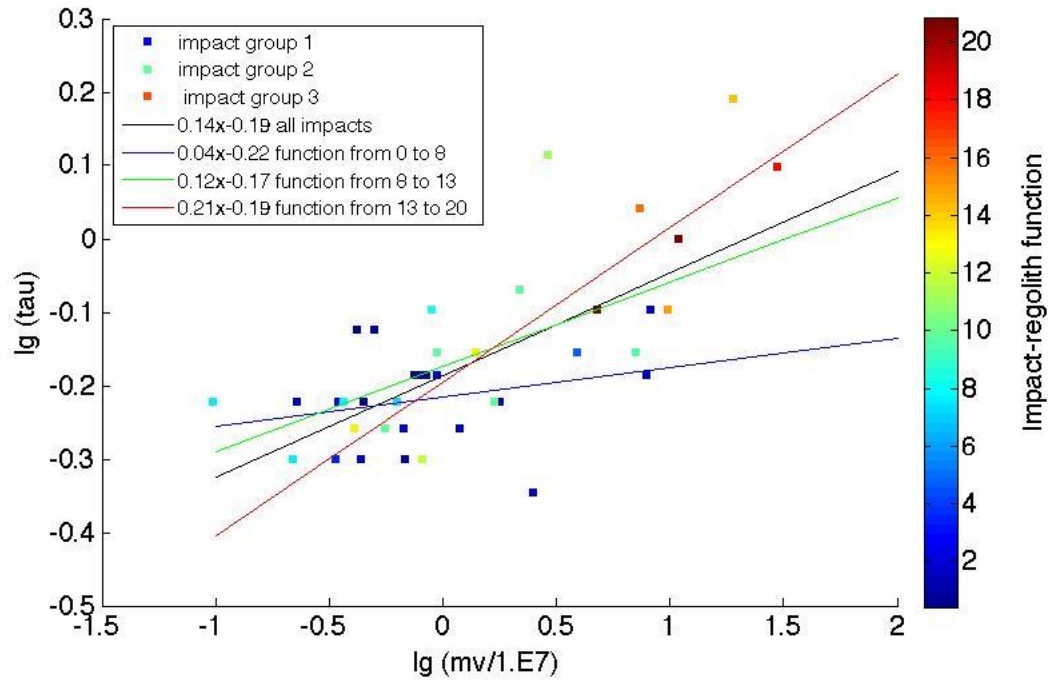


Fig. 4. Trade-off between the impact duration, momentum transfer of the impactor and the impact-regolith thickness at the observed impact locations. The estimated impact-regolith thickness (a proxy for the impact-regolith function that is proportional to the real regolith thickness, as described in Section 4) is shown by color. Color lines display the least squares solution for the cutoff frequency for three groups of impacts depending on the regolith thickness in the vicinity of the impact: (1) blue line, impact-regolith function is between 0 and 8; (2) green line, impact-regolith function is between 8 and 13; (3) red line, impact-regolith function is between 13 and 20. The RMS errors are 13%, 25%, 14% and 16% for Group1, Group2, Group3, respectively. Black line is a fit for all Apollo-recorded impacts considered in this study, with the RMS error of 16%.

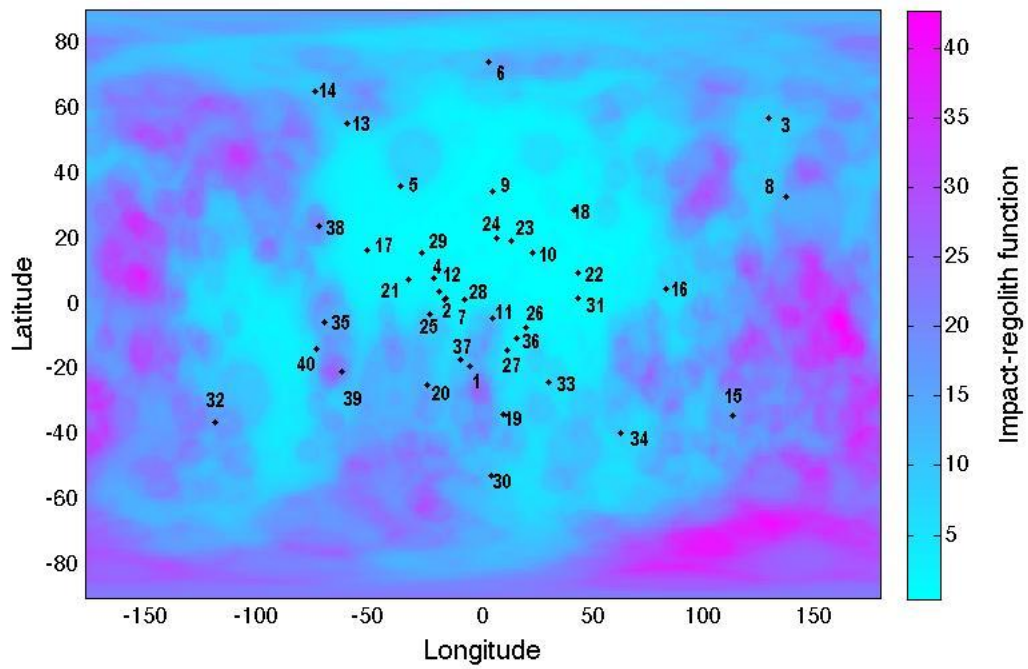


Fig. 5. Locations of the meteoroid impacts are shown on the map of the modeled impact-regolith function. White points represent the contour of the GRAIL coverage from Wieczorek et al. (2013).

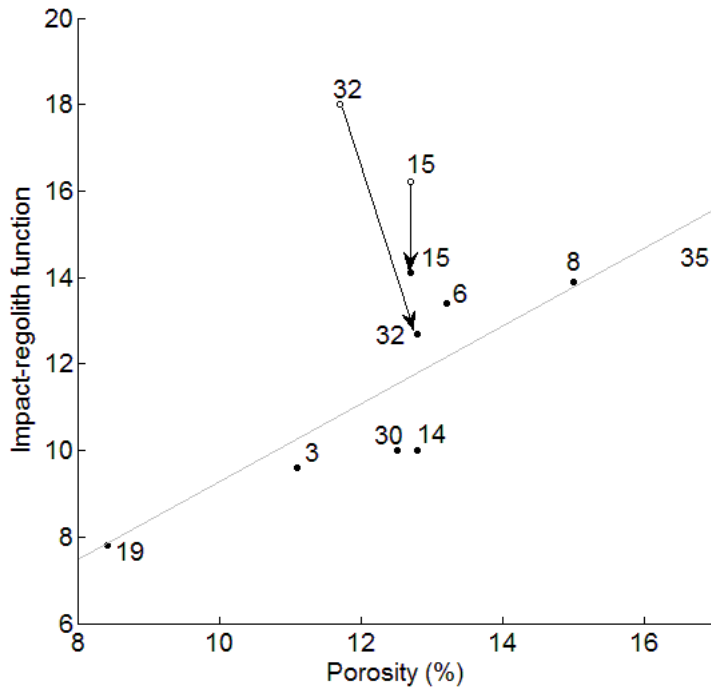


Fig. 6. The correlation between the porosity map of GRAIL and modeled impact-regolith function. Error bars show the variability of the impact regolith function within the impact location error ellipses. Black line is the least-squares solution for all impacts, with the RMS error of 27%.

Table 1. Location and seismic parameters of the meteoroid impacts analyzed in this study

Impact	Date (year, month, day, hour, min)	Lat	Long	mv (kg m/s)	τ (s)
1	1971/05/12, 09:34	-18.9	-5.9	8.18E+06	0.50
2	1971/05/23, 22:09	1.7	-16.6	2.48E+07	0.45
3	1971/06/27, 18:44	57.0	129.4	7.11E+07	0.70
4	1971/07/27, 11:34	7.8	-21.9	3.49E+06	0.60
5	1971/10/20, 17:57	36.1	-36.9	3.89E+07	0.70
6	1972/01/04, 06:24	74.1	2.5	1.38E+07	0.70
7	1972/05/13, 08:35	1.5	-17.1	8.22E+07	0.80
8	1972/07/17, 21:45	32.8	137.6	1.89E+08	1.55
9	1972/07/31, 17:57	34.5	4.8	1.76E+07	0.60
10	1972/08/29, 22:48	15.8	22.9	6.87E+06	0.50
11	1972/09/21, 00:37	-4.1	4.5	2.19E+06	0.50
12	1972/11/14, 19:14	3.9	-19.5	2.28E+06	0.60
13	1972/11/19, 18:13	55.4	-61.3	1.69E+07	0.60
14	1972/12/02, 07:47	65.1	-75.7	9.50E+06	0.70
15	1973/04/23, 13:45	-34.1	113.0	7.39E+07	1.10
16	1973/07/04, 02:35	4.9	83.0	9.03E+06	0.80
17	1973/08/01, 10:51	16.6	-52.1	5.03E+06	0.75
18	1973/09/26, 20:37	28.7	41.1	8.49E+06	0.65
19	1973/10/21, 05:21	-33.9	9.1	3.74E+06	0.60
20	1973/12/24, 09:54	-24.8	-25.1	4.11E+06	0.55
21	1974/04/19, 18:23	7.4	-33.6	4.41E+06	0.50
22	1974/06/30, 17:34	9.5	43.3	7.51E+06	0.65
23	1974/07/06, 14:03	19.5	12.8	4.53E+06	0.60
24	1974/07/17, 11:54	20.3	6.5	4.24E+06	0.75
25	1974/09/23, 11:42	-2.9	-24.0	9.83E+05	0.60
26	1974/11/21, 13:05	-7.3	19.9	1.20E+07	0.55
27	1974/12/09, 09:19	-14.1	11.0	3.40E+06	0.50
28	1974/12/15, 08:57	1.6	-8.2	6.75E+06	0.55
29	1975/03/01, 04:07	15.8	-27.2	7.92E+06	0.65
30	1975/03/05, 21:41	-52.4	4.2	2.16E+07	0.85
31	1975/04/12, 04:10	2.0	43.2	7.87E+07	0.65
32	1975/05/04, 09:55	-36.4	-121.3	3.02E+08	1.25
33	1975/10/06, 12:47	-23.9	29.8	6.31E+06	0.60
34	1976/01/13, 07:05	-39.4	62.8	7.10E+07	0.70
35	1976/01/25, 15:59	-5.6	-71.5	9.93E+07	0.80
36	1976/05/16, 12:37	-10.4	15.3	9.48E+06	0.65
37	1976/05/28, 05:52	-16.8	-10.0	5.58E+06	0.55
38	1976/11/14, 23:05	23.8	-73.9	1.14E+08	1.00
39	1977/04/17, 23:26	-20.5	-63.8	4.77E+07	0.80
40	1977/06/28, 22:14	-13.5	-75.3	2.89E+07	1.30

Table 2. The crater diameter and depth, the corresponding excavation mass and volume of material ejected in these craters, as calculated using the method of Holsapple (1993). The calculation includes the target density of 2100 kg/m³, the impactor density of 3000 kg/m³, the impactor velocity of 20 km/s, and the average ejecta angle at 45⁰.

Crater diameter (km)	Depth (km)	Exc. Mass (kg)	Exc. Volume (m ³)
10	2.72	1.58E14	9.39E10
20	5.45	1.26E15	7.51E11
30	8.17	4.26E15	2.54E12
40	10.90	1.01E16	6.01E12
50	13.62	1.97E16	1.17E13
60	16.34	3.41E16	2.03E13
70	19.06	5.41E16	3.22E13
80	21.79	8.08E16	4.81E13
90	24.51	1.15E17	6.85E13
100	27.23	1.58E17	9.39E13
500	136.0	1.97E19	1.17E16

Table 3. The distribution of ejecta volume (in %) for different diameter craters.

Crater diameter (km)	Excavation volume (m ³)	75%	50%	25%	10%	5%
10	9.39E10	3.7 km	6 km	14 km	42 km	97 km
20	7.51E11	7 km	11 km	27 km	80 km	190 km
100	9.39E13	33.6 km	55 km	130 km	390 km	890 km
500	1.17E16	164 km	270 km	620 km	1885 km	4370 km